Integrated and Superaerophilic Ni-O-C Electrode enables Fast and Stable Electrochemical H2O2 Production for Electro-Fenton-like Process

Wenwen Xu
Ningbo Institute of Materials Technology and Engineering, Chinese Academy of Sciences
https://orcid.org/0000-0001-7588-5016

Zheng Liang
Shanghai Jiao Tong University https://orcid.org/0000-0001-9137-0338

Shun Gong
Ningbo Institute of Materials Technology and Engineering, Chinese Academy of Sciences

Baoshan Zhang
Ningbo Institute of Materials Technology and Engineering, Chinese Academy of Sciences

Linfeng Su
Ningbo Institute of Materials Technology and Engineering, Chinese Academy of Sciences

Hui Wang
Ningbo Institute of Materials Technology and Engineering, Chinese Academy of Sciences

Xu Chen
Ningbo Institute of Materials Technology and Engineering, Chinese Academy of Sciences

Nana Han
Department of Chemistry and Materials Science, Aalto University School Chemical Engineering

Ziqi Tian
Ningbo Institute of Industrial Technology

Tanja Kallio
Aalto University https://orcid.org/0000-0001-6671-8582

Liang Chen (chenliang@nimte.ac.cn)
Ningbo Institute of Materials Technology and Engineering, Chinese Academy of Sciences

Zhiyi Lu
Ningbo Institute of Materials Technology and Engineering, Chinese Academy of Sciences

Xiaoming Sun
Beijing University of Chemical Technology

Article

Keywords: wastewater treatment, hydrogen peroxide (H2O2)

Posted Date: February 9th, 2021

DOI: https://doi.org/10.21203/rs.3.rs-200180/v1

Abstract

Fast and stable production of hydrogen peroxide (H_2O_2) through electrochemical pathways is crucial for wastewater treatment applications. With this objective, herein we report an integrated and superaerophilic electrode composed of atomically dispersed Ni-O-C sites enriched carbon nanosheets (IS-NiOC electrode) for electrochemical oxygen reduction to produce H_2O_2. Both experimental and theoretical results have proven that atomically dispersed Ni-O-C sites enable a low overpotential (260 mV at 0.1 mA cm^{-2}) and high selectivity (> 90% at 0.0 ~ 0.5 V *vs.* RHE) in neutral electrolyte. Compared with a commercial gas-diffusion electrode, the IS-NiOC electrode offers stronger affinity to oxygen bubbles and more robust three-phase contact points, resulting in high current density (~ 106 mA cm^{-2} at 0.25 V *vs.* RHE) and superior stability (~ 200 h). These merits allow the application of the IS-NiOC electrode in an electro-Fenton-like process, which enables fast degradation of representative organic pollutants in both steady state and flow state.

Introduction

Hydrogen peroxide (H_2O_2) is an environmentally friendly and highly efficient oxidant with a wide range of applications in fields of wastewater purification, medical treatment and industrial synthesis[1–4]. At present, over 99% of H_2O_2 is produced by anthraquinone oxidation process; however, this process requires complex and large-scale infrastructure, generates a substantial volume of waste chemicals, and induces potential hazards in transport or store of the high concentration products[5–9]. For these reasons, an alternative route for small-scale on-site generation is urged to exploit. Direct electrochemical synthesis of H_2O_2 by oxygen reduction reaction via a two-electron pathway (2e ORR) has gained a satisfactory solution to address the issues associated with the anthraquinone process due to its low resource consumption, convenience, and green initiative[8,10–14]. In practice, 2e ORR has already been successfully applied in electro-Fenton(EF)/electro-Fenton-like(EF-like) reactions[15–17], which belong to economical advanced oxidation processes[18–20] for hazardous organic pollutants degradation.

In order to achieve fast and stable H_2O_2 generation by an electrochemical method, catalytic electrodes with high current density at a low overpotential, high selectivity and excellent stability are desperately needed[2,21–24]. Previous studies have already identified various active catalysts, including noble metals and their alloys[25–28], active carbonaceous materials[11,29–32] and transition metal-doped carbon materials[33–36]. In contrast to tremendous progress in seeking for active catalysts, there are very limited efforts devoted to investigate advanced electrode architectures, which is equally important and nonnegligible as efficient electrode architectures can simultaneous accelerate electron and reactant transport rate.[37–42] The general strategy to solve this problem is employing a Teflon-treated carbon fiber paper (TCFP) as the substrate to increase three-phase contact point (TPCP) by constructing gas-diffusion layer, as shown in Fig. 1a. However, the *in-situ* generated H_2O_2 on an electrode surface would easily oxidize the carbon-based catalysts/substrates, and eventually destroy the gas diffusion channels and

operation stability. Direct construction of active materials into micro-/nanostructures on conductive substrates to form integrated electrodes may reinforce the gas diffusion channels to against the destruction.[38,39,43,44] As schemed in Fig. 1b, we hypothesize that the integrated and superaerophilic electrode establishes a dense and thick gas diffusion layer that can mitigate the H_2O_2 corrosion process.

Following this line, herein we demonstrated a nickel-incorporated oxidized carbon nanosheets arrays on carbon-fiber paper (CFP) for electrochemical H_2O_2 production. The nickel-incorporated oxygen-doped carbon catalyst (NiOC) exfoliated from CFP exhibited an outstanding intrinsic activity with an onset potential of ~ 0.5V *vs*. RHE and high selectivity (> 82%) over a wide potential range of 0.0 ~ 0.5V *vs*. RHE in neutral electrolyte. Proper surface modification of the NiOC electrode surface achieved strong affinity to gas bubbles, resulting in the fabrication of an integrated and superaerophilic NiOC electrode (IS-NiOC electrode) with robust and enriched TPCPs. Combining the advantages of the catalyst and surface property, the IS-NiOC electrode exhibited large current density (> 100 $mA{\cdot}cm^{-2}$) at 0.25V *vs.* RHE and remarkable selectivity (> 90% at 0.0 ~ 0.5 V *vs.* RHE). More importantly, compared with a traditional electrode made by a drop-casting method (D-NiOC electrode, < 10 h stability), the IS-NiOC electrode possessed superior operation stability (~ 200 h) for electrochemical air reduction to produce H_2O_2. We also demonstrated the application of the IS-NiOC electrode in an EF-like process, which realized fast degradation of representative organic pollutants.

Results

Synthesis and characterizations of the IS-NiOC electrode. The IS-NiOC electrode was synthesized by a multi-step process, as schemed in Supplementary Fig. 1a. Firstly a conventional solvothermal method was employed to synthesis $Ni(OH)_2$ nanosheet (average size and thickness of ~ 1 μm and ~ 50 nm, respectively) arrays on CFP, as shown in Supplementary Fig. 1b. Afterwards, the $Ni(OH)_2$ nanosheet arrays were *in situ* transformed to NiOC catalyst (Fig. 1c, XRD can be seen in Supplementary Fig. 1c) with hierarchical and porous architecture by carbonizing polyoxyethylene (PEO) at a high temperature. Further, the NiOC electrode was modified by a specific concentration of fluorine-based polymers to achieve a superaerophilic surface. To demonstrate the structural advantage, the exfoliated NiOC catalyst was drop-casted on TCFP (D-NiOC electrode) as the contrast electrode. It was revealed that, once an individual air bubble (~ 50 μL) touched the electrode surface, about ~ 3.8s was needed for the bubble to spread out on D-NiOC electrode (Fig. 1g and Supplementary Movie 1) while the required time shrunk to ~ 0.8 s for the IS-NiOC electrode (Fig. 1e and Supplementary Movie 2), clearly demonstrating a much stronger affinity of the IS-NiOC electrode towards air bubbles. This phenomenon was attributed to the superaerophilic layer under neutral electrolyte (1 M Na_2SO_4), which could build up a numerous of sturdy air pockets for coalescing with bubbles.

Transmission electron microscopy (TEM, Fig. 2a) revealed that the final product was mainly composed of stubby carbon nanotubes, and high-resolution TEM image (Supplementary Fig. 2) illustrated that Ni nanoparticle (lattice spacing: 0.208 nm) was encapsulated in the multilayered carbon shell (lattice

spacing: 0.367 nm) and located at the tip area of stubby nanotubes. It should be noted that the Ni nanoparticles cannot be washed out even using strong acids. The atomic dispersion of Ni sites on NiOC was confirmed by aberration-corrected high-angle annular dark field scanning transmission electron microscopy (HAADF-STEM, Fig. 2b) where the bright dots corresponding to Ni single-atom sites (marked by white circles, size of the bright spots if ca. 0.2 nm) were homogenously distributed throughout the entire sample. Elemental mappings results further confirmed the homogeneous distribution of Ni, O and C species across the tubular structure (Fig. 2c) despite the presence of inevitable Ni nanoparticles.

Closer inspection on the electronic structure promotes the deep understanding of structure-activity relationship. X-ray photoelectron spectroscopy (XPS) was firstly performed, and the results (Supplementary Fig. 3a) further proved the presence of Ni, O and C elements in NiOC electrode. The existence of fluorine (F) (Supplementary Fig. 3b) in IS-NiOC electrode confirmed the successful modification by polytetrafluoroethylene (PTFE). The deconvoluted spectrum of nickel 2*p* (Fig. 2d) illustrated the coexistence of metallic and oxidation state nickel[45–47], and the deconvoluted spectrum of oxygen 1*s* (Fig. 2e) revealed that oxygen existed in three forms including C-O-C (533.0 eV)[11,48], C = O (531.96 eV)[11,48] and Ni-O-C (530.82eV)[48]. Compared with oxidized carbon material (O-C) without Ni incorporation (Supplementary Fig. 4, synthesis details in SI), the additional Ni-O-C peak indicated that the atomically dispersed Ni sites were mostly coordinated with oxygen. The oxidation state of Ni was also examined by the position of rising edge of Ni K-edge X-ray absorption near edge structure (XANES). As shown in Fig. 2f, the Ni K-edge XANES spectra of NiOC contained different characteristic features to Ni-foil and NiO[49]. The inset in Fig. 2f highlighted that the rising edge of Ni K-edge XANES spectra was located between those of Ni foil and NiO, clearly showing the dominant unique electronic structure of Ni-O-C.

2e ORR performance of IS-NiOC electrode. The electrochemical H_2O_2 production in neutral media is of practical significance as it can accommodate high concentration of H_2O_2 with negligible decomposition[2,50]. The intrinsic 2e ORR performance of the as-grown NiOC (exfoliated from the NiOC electrode) was firstly evaluated by casting the ink onto the rotating ring disk electrode (RRDE, collection efficiency is ~ 0.35, Supplementary Fig. 5) in 0.1 M phosphate buffered saline (PBS). The oxygen reduction current was measured on a disk electrode (black solid line in Fig. 3a), and the amount of formed H_2O_2 was simultaneously quantified by the Pt ring electrode (black dashed line in Fig. 3a). The corresponding H_2O_2 selectivity was plotted (black line) in Fig. 3b as a function of potential. For comparison purposes, oxidized carbon (O-C) catalyst without Ni incorporation was synthesized and tested under the same condition. Notably, the NiOC catalyst possessed an onset potential of ~ 0.50 V (*vs.* RHE) at 0.01mA·cm^{-2} and achieved selectivity of > 82.8% at a wide potential range of 0-0.50V (*vs.* RHE) in neutral media. Analogously, the O-C catalyst exhibited a similar selectivity at a narrower potential range (0 ~ 0.33 V *vs.* RHE), but a strong distinction occurred on the overpotential (Δ = 0.17 V). In addition, a faster ORR kinetics was found on the NiOC catalyst than that of O-C catalyst, as reflected in Tafel slopes (118.2 mV dec^{-1} for NiOC and 161.0 mV dec^{-1} for O-C, Supplementary Fig. 6). In view of the former XPS and XANES analysis, we thus drew a conclusion that such a huge ORR performance disparity was

attributed to the presence of atomically-dispersed nickel in catalyst. Moreover, the NiOC catalyst was superior to those of reported carbon-based catalysts (O-CNTs[11], Fe-CNT[33], g-N-CNTs[51], summarized in Table S1) and represented an outstanding activity and selectivity of the catalyst for 2e ORR in neutral media.

To understand the intrinsic high activity of NiOC system, DFT calculations were performed. For the 2e ORR, there are two reaction steps[52]:

$$* + O_2 + H_2O + e^- \rightarrow *OOH + OH^- \quad (1)$$

$$*OOH + e^- \rightarrow HO_2^- + * \quad (2)$$

where the asterisk (*) represents the active site. As shown in Fig. 3c, the energy of *OOH species on C-O surface was related to a thermodynamical barrier of +0.77 eV under external potential of 0.70 eV. Once the Ni single atom coordinates to oxygen forming the Ni-O-C bond, the binding between hydroperoxide group and carbon is significantly strengthened. Generation of H_2O_2 possesses a smaller barrier of -0.53 eV. Herein the Ni-O-C system should exhibit an improved performance than pristine C-O system. Furthermore, Bader charge analysis shows that the atomic charge of the potential active carbon site changes from positive (0.77 |e|) to negative (-0.53 |e|) after the Ni coordination with O, indicating that electron transfers from nickel to carbon substrate. As a result, the accumulation of electron facilitates the reduction of oxygen to generate H_2O_2.[53]

The superaerophilic property of an electrode has already been demonstrated effective in accelerating the gas diffusion process, thereby greatly enhancing the current increasing rate in diffusion region[39]. In this case, a fast-current increase rate as well as a large current density was observed in the IS-NiOC electrode by virtue of the advantages of catalyst and architecture. To evaluate the performance under high current density, a steady state ORR test was performed in with continuous oxygen bubbling by using H-Cell (as shown in Supplementary Fig. 7). The D-NiOC electrode with weaker affinity to gas bubbles was also tested for comparison. The typical ORR polarization curves with IR-correction of D-NiOC electrode and IS-NiOC electrode in neutral media were shown in Fig. 3d. The IS-NiOC electrode displayed an ultrahigh ORR performance with a rapid and stable current increase (~75 $mA \cdot cm^{-2}$ per 100 mV) and a large current density (~122 $mA \cdot cm^{-2}$ at 0.2 V *vs.* RHE, with IR correction). On the contrary, the D-NiOC electrode exhibited a limited current density (37.9 $mA \cdot cm^{-2}$ at 0.2 V *vs.* RHE, with IR correction) and slower current increasing rate (~17.6 $mA \cdot cm^{-2}$ per 100 mV). This phenomenon was attributed to lack of hierarchical architecture on D-NiOC electrode (as shown in Supplementary Fig. 8a), which weakened the interaction with gas bubbles. Moreover, benefiting from the superaerophilic nanostructure, the unique surface of IS-NiOC electrode could guarantee an unobstructed channel for gas reactants by constructing the robust TPCP and thick gas transfer channel.

Tafel analysis (Fig. 3e) illustrated that the IS-NiOC electrode provided a wider potential and current range (Δ= 0.1347 V, 0-15.46 mA cm^{-2}) than that of D-NiOC electrode (Δ= 0.071 V, 0-8.55 mA cm^{-2}) for linear portion of the curve, indicating that the gas diffusion process on IS-NiOC electrode was much faster than that of D-NiOC electrode. For the IS-NiOC electrode, the corresponding selectivity and production rate of H_2O_2 under different potential (without IR-correction) in neutral medias were shown in Fig. 3f, where a high H_2O_2 selectivity of 90.4% and H_2O_2 production rate of 59.3 mg·cm^{-2} h^{-1} at 0 V vs RHE were observed. This performance enhancement was also applicable in alkaline electrolyte (1 M KOH), where the IS-NiOC electrode exhibited a large current density (~250 mA·cm^{-2} at 0.3 V *vs.* RHE, without IR correction) and splendid H_2O_2 selectivity (~95%), as shown in Supplementary Fig. 9. The IS-NiOC electrode can also reduce the oxygen in air with relatively lower concentration to form H_2O_2 in a neutral system, where the working electrode was floated horizontally on the surface of the electrolyte (as shown in Supplementary Fig. 10). The up-side surface can absorb air as the reactants and simultaneously release the liquid products from the down-side surface. For the IS-NiOC electrode, the 2e ORR current density in air atmosphere decreased to ~20% of that in oxygen atmosphere (Fig. 3g), which was consistent with the changing of oxygen concentration. In addition, the performance of IS-NiOC electrode and D-NiOC electrode in air got a similar tendency with those in oxygen atmosphere, as shown in Fig. 3h and 3i. The Tafel plots (Supplementary Fig. 11) indicated that, compared with the ORR potential of IS-NiOC electrode in pure oxygen, a negative potential shift (55mV) was observed for the same electrode in air. This potential shift was very close to the theoretical value of 46 mV (based on Nernst Equation, more details can be found in Supporting Information). The Tafel slopes of IS-NiOC electrode were 93.4 mV·dec^{-1} and 92.3 mV·dec^{-1} in air and pure oxygen, respectively, indicating that the decrease of oxygen concentration did not affect the ORR kinetics significantly.

It was found that the ORR performance of the IS-NiOC electrode was highly dependent on the PTFE-modification parameters, as shown in Fig. 3j. A very limited current density (1 mA cm^{-2} at 0V) was observed on the electrode without PTFE-modification, mainly because of the weak oxygen bubble adhesion capability (Supplementary Fig.12). The IS-NiOC electrode soaked in a diluted PTFE concentration (0.05 wt%) cannot afford a strong oxygen bubble adhesion, whereas increasing the concentration would impede the electron transport. These two metrics should be simultaneous optimized for achieving a superior current density. After intensive experimental efforts, an optimal PTFE concentration came to 0.1 wt%. More noteworthy, a significantly prolonged 2e ORR stability was observed on IS-NiOC electrode when performing air reduction in neutral system. Under the same test condition, the IS-NiOC electrode (modified by 0.1 wt% PTFE) could continuously produce H_2O_2 (~25 mA·cm^{-2}) for over 200 h (navy plots in Fig. 3k), while the promising initial current density was only maintained for a few hours (<10 h) for D-NiOC electrode with the same mass loading (dark red plots in Fig. 3k). It is worth mentioning that, the H_2O_2 selectivity was kept at a stable value (~90%) during all the processes for both IS-NiOC and D-NiOC electrodes, indicating that the decay of the D-NiOC electrode was not caused by catalysts degradation. In a deeper analysis, it is revealed that both the IS-NiOC electrode and D-NiOC electrode suffered from the surface corrosion from the H_2O_2 production since the surface liquid contact

angles (LCAs, Supplementary Fig. 13) got a variable decrease after a period of running. The significant difference is attributed to the robust TPCP of IS-NiOC electrode which could alleviate the corrosion to a great extent. To validate this assumption, an IS-NiOC electrode with a thinner gas film (soaked in 0.1 wt% PTFE for shorter time, ~8 min) was subject to a stability running. As expected, the latter one showed a slightly worse stability (red plots in Supplementary Fig. 14). Based on the above information, we believe that the robust gas diffusion layer plays a vital role in stability enhancement. The surface properties of IS-NiOC electrode and D-NiOC electrode before and after long-term reaction were thus characterized in detail. The air diffusion side for both IS-NiOC and D-NiOC electrodes is still intact after long-term testing, indicating that oxygen can be continuously diffused into the electrode. However, as for the water diffusion side, the IS-NiOC and D-NiOC electrodes show a considerable difference in the affinity to water. As shown in Supplementary Fig. 13, a significant decrease on LCA (from 150.8° to 53.9°) was found for the D-NiOC electrode after long-term testing, while a slight decrease (from 154.2° to 119.5°) was observed in the LCAs of the IS-NiOC electrode. Considering the ORR reaction only occurred at TPCP, the fast-current density degradation was directly caused by TPCP vanishment.

EF-like performance of IS-NiOC electrode. Electrochemical advanced oxidation processes (EAOPs) have attracted substantial attention owing to the environmental versatility, high efficiency and safety[54]. Among all the EAOPs, the EF process is most popular, in which the oxidant (H_2O_2) is formed *in-situ* from oxygen at the cathode surface in acidic solutions. However, generation of large values of iron-containing sludge and limited operating pH range (an optimal run is performed at pH ~3) of EF process urges the development of EF-like process which can be operated in a completely heterogeneous and neutral system.[55,56] Besides stable and fast H_2O_2 generation, a desirable electrode should also possess the capability to activate H_2O_2 to degrade organic pollutants (i.e. Fenton-like process)[57-59]. It is reported that H_2O_2 can be activated to reactive oxygen species (ROS) along with the valence state change of Ni in Ni-based catalysts[60]. In this case, we thus evaluated the Fenton-like performance of NiOC catalyst in neutral system and observed that NiOC catalyst exhibited a more effective degradability compared with that of O-C catalyst under the same experiment conditions (Supplementary Fig. 15). Thus, combining the advantages of rapid H_2O_2 production and Fenton-like activity in neutral system, the IS-NiOC electrode is supposed to show a high EF-like performance.

To evaluate the EF-like performance, a steady-state three-electrode system enabling on-site H_2O_2 production and *in-situ* organic (Indigo) degradation was constructed, as shown in Fig. 4a. A Nafion membrane was adapted to separate the cathode and anode reaction, which could avoid the oxidation of generated H_2O_2 on the anode surface. The IS-NiOC electrode was employed as the cathode to reduce oxygen to H_2O_2, which was further converted to ROS assisted with NiOC catalyst. As shown in Fig. 4b and 4c, the IS-NiOC electrode took 60, 40 and 24 minutes to complete degrade Indigo (50 ppm in 15 ml) under the current densities of 10, 20, and 50 mA cm^{-2}, respectively. In order to simulate the industrial pollutants degradation process, a two-electrode device (without any membrane) with an electrolyte circulating system was constructed, as schemed in Figure 4d and Supplementary Fig. 16. The IS-NiOC electrode was

employed as the cathode and the dimensionally-stable boron-doped diamond (BDD) electrode was used as the anode. The employment of BDD electrode enables accelerated organics degradation process as it is well-known to produce strong oxidant (hydroxyl radical, ·OH) through the discharge of water at high oxidation potentials. The oxygen gas flowed over the anode surface to provide reactant gas, and 50 mL electrolyte containing representative organic pollutant (50 ppm bisphenol A in 0.05 M Na_2SO_4) flowed through the channel. As shown in Fig. 4e, both the BPA and total organic carbon (TOC) removal rate increased under an operation current of 40 mA (the operation voltage is almost constant at ~3.3 V). After 8 hours reaction, the BPA and TOC removal rate reached ~95% and ~ 62%, respectively. Overall, the results demonstrated the great application potential of IS-NiOC electrode in EF-like process for wastewater treatment.

Discussion

In conclusion, we have successfully fabricated an integrated and superaerophilic electrode with a hierarchical architecture of NiOC catalyst for fast and stable H_2O_2 electrochemical generation in neutral media. The NiOC catalyst was demonstrated effective in selective production of H_2O_2 from electrochemical oxygen reduction, and the superaerophilic surface property further accelerated both oxygen diffusion and electron transport rates, thereby greatly improving the 2e ORR current density and stability. We also demonstrated the application of IS-NiOC electrode in EF-like process, which realized effective degradation of representative organic pollutants. The concept and principles in this work should be applicable for designing electrochemical H_2O_2 production electrodes in the future.

Method

Synthesis of IS-NiOC electrode: The IS-NiOC was fabricated by a three-step method. Firstly, $Ni(OH)_2$ nanosheets were constructed on microporous carbon fiber paper (CFP, fuel cell store) by solvothermal method. In a typical procedure, $Ni(NO_3)_2{\cdot}6H_2O$ (1 mmol) and $CO(NH_2)_2$ (10 mmol) were dissolved in 36 mL of methanol to form a clear solution by continuous stirring. CFP which was pre-treated by oxygen plasma and the as-obtained solution were transferred to a 40 mL Teflon-lined stainless-steel autoclave. Then, the autoclave was kept at 120℃ for 12 hours, and then allowed to cool down to room temperature naturally. Thus, the $Ni(OH)_2$ nanosheet arrays on CFP were obtained and subsequently rinsed with distilled water and ethanol each for 5 min with the assistance of ultrasonication, and dried at 80℃ for 2 hours. Secondly, the $Ni(OH)_2$@CFP nanosheet arrays was propped on a porcelain boat which was filled with polyoxyethylene (PEO, Mv~10,000) powder and the porcelain boat was put into the tube furnace with an Ar gas flow (40 sccm). The tube furnace was heated up to 900 ℃ in 90 min and was held at that temperature for 3 hours to carbonize the PEO and grow carbon materials in-situ on the CFP. The distance between the CFP and the PEO powder was kept between 0.5 and 1 cm, and the PEO amount was kept between 0.5 and 2 g. Lastly, the as-prepared NiOC electrode was soaked in PTFE (0.1 wt%) for 10 min, and then heated at 350 ℃ for 30 min in air atmosphere. The mass loading of the catalyst was measured as ~3mg cm^{-2}.

Synthesis of D-NiOC electrode: The same mass loading (~3mg·cm^{-2}) of the NiOC catalyst was fabricated by the drop-casting method. Specifically, the NiOC catalyst was dispersed in ethanol solution with a concentration of 1 mg mL^{-1}. Then the solution with NiOC was loaded on PTFE modified CFP by drop-casting.

Synthesis of O-C catalysts: 1g active carbon and 1g PEO was put into the tube furnace after mixing up, the tube furnace was heated up to 900℃ in 90 min and held for 3 hours under Ar atmosphere.

Characterizations: The structural information of sample was characterized using field-emission SEM (Zeiss SUPRA 55) operating at 20 kV and high-resolution TEM system (JEOL 2100) operating at 200 kV. XPS spectrum was carried out by using a model of ESCALAB 250. X-ray powder diffraction patterns were recorded on an XRD (Rigaku D/max 2500) at scan rate of 10° min^{-1}. The aberration-corrected HAADF-STEM measurements were taken on a JEM-ARM200F instruments at 200 keV. X-ray absorption spectroscopy (XAS) was conducted at the Shanghai Synchrotron Radiation Facility (SSRF).

Surface Characterizations to Oxygen Bubbles: This study characterized the wetting ability of the electrodes by measuring the contact angles of a Na_2SO_4 solution using Optical contact angle and Surface/interfacial tension measuring system (OSA 60G, LAUDA Scientific, Germany). For these experiments, 50 μL of the electrolyte were dropped on the electrode surface, and the LCA was measured in ambient air at room temperature. The air-bubble CA with the volume of ~50 μL was measured by the captive-bubble method.

Electrochemical RRDE Characterizations: For the preparation of the catalytic electrodes, the NiOC catalysts were dispersed in ethanol to achieve a catalyst concentration of ~5 mg·mL^{-1} with 5 wt% Nafion solution. After sonication for 60 min, 10 μL of the catalyst ink was drop-dried onto a glassy carbon disc (area: 0.247 cm^2, PINE). The electrochemical tests were performed in a computer-controlled CHI working station (Shanghai CHENHUA) with a three-electrode cell at room temperature. The glass carbon electrode loaded with catalyst was used as the working electrode. A graphite rod and a Ag/AgCl were used as the counter and reference electrode, respectively. 0.1 M phosphate buffered saline was chosen as the electrolyte. The ORR activity and selectivity were investigated by polarization curves and rotating ring-disk electrode measured in oxygen-saturated electrolyte at a scan rate of 10 mV·s^{-1}.

H_2O_2 selectivity of the NiOC catalyst on the rotating ring-disk electrode was calculated based on the current of both disc and ring electrodes (equation (1)). A potential of 1.2 V (versus RHE) was applied on the ring of the working electrode at a speed of 1600 r.p.m. during the entire testing process.

$$H_2O_2 \text{ yield: } H_2O_2\ (\%) = 200 \times \frac{I_R/N}{I_D + I_R/N} \qquad (1)$$

where I_R is the ring current, I_D is the disk current, N is the collection efficiency (experimental calibration (~0.35) in Supporting Information (Supplementary Fig. 5)).

Practical Electrochemical Characterizations: To avoid the negative effect of Ohm resistance, an open system was employed to measure the current density (as shown in Supplementary Fig. 7). Practical ORR selectivity was performed in a two-compartment cell with Nafion 117 membrane as separator. Both the cathode compartment and the anode compartment were filled with the same electrolyte (20 mLof 1 M Na_2SO_4 or 1 M KOH). The electrolyte in anode compartment was saturated by oxygen gas, and 1 cm^2 electrode (IS-NiOC electrode, or D-NiOC electrode) was soaked in electrolyte as the working electrode. A Ag/AgCl or Hg/HgO electrode was employed as the reference electrode for neutral and alkaline systems, respectively. A graphite rod was placed in the cathode compartment as the counter electrode. To evaluate the H_2O_2 selectivity, the electrode was operated for several minutes under a constant potential, then the electrolyte was collected to quantify the H_2O_2 concentration. Theoretically, 1 C of electric quantity will produce 8.82 ppm H_2O_2 (equation (2)) under this condition (20 mL electrolyte).

$$\frac{1C \times 6.25 \times 10^{18} e/C}{6.02 \times 10^{23}\, e/mol \times 2} \times \frac{34 \frac{g}{mol}}{20\, mL} = 8.82 \times 10^{-6} \frac{g}{mL} = 8.82\, ppm \quad (2)$$

Electrochemical Air Reduction Characterizations: The electrochemical air reduction was performed by using the home-made device (as shown in Supplementary Fig. 10). A graphite rod and a Ag/AgCl were used as the counter and reference electrode, respectively. A flowing 1 M Na_2SO_4 solution was employed as the electrolyte. The selectivity was performed by calibrating the collected electrolyte.

Fenton-like degradation: A 50 mL of 10 mg/L RhB solution and 10 mg catalyst were transferred into the conical flask, as shown in Supplementary Fig. 15. The conical flask was kept under sonification until the catalyst homogeneous dispersion. Then, the conical flask was fixed on shaker and keep shaking for 12 hours to complete adsorption. 3 mL of 30 wt% H_2O_2 was put into the solution. To analysis the concentration of the organic, 1 mL degradation solution was extraction, and 1 mL of 0.5 M Na_2SO_3 was injected to stop the oxidizing of the remaining H_2O_2. After the centrifugation, the concentration was quantified by the UV-vis.

Steady State of electro Fenton-like degradation: An H-Cell was employed as the reaction device, and Nafion 117 membrane as the separator. Both the cathode compartment and the anode compartment were filled with the same electrolyte (20 mL of 0.05 M Na_2SO_4 and 50 ppm Indigo). The electrolyte in anode compartment was saturated by oxygen gas, and 1 cm^2 of IS-NiOC electrode was soaked in electrolyte as the working electrode. A Ag/AgCl was employed as the reference electrode and a graphite rod was placed in the cathode compartment as the counter electrode. The reaction current was set as 10, 20 and 50 mA, to collect the degrade tendency, 0.5 mL of the reaction solution was extracted and mixed with 0.5 mL Na_2SO_3. The concentration of Indigo was ensured by the UV-vis.

Flow State of electro Fenton-like degradation: The two-electrode and flow-state device was home-made, see details in Supplementary Fig. 16. The IS-NiOC electrode was employed as the cathode and the BDD electrode was employed as the anode (reaction on BDD electrode was as eq (3)). The working area for anode was 2*2 cm^2, and the distance between cathode and anode was 2 mm. The oxygen gas flowed in and out over the surface of the anode, and the electrolyte was pumped through the channel from the cathode by the peristaltic pump.

$$BDD + H_2O \rightarrow BDD(\cdot OH) + H^+ + e^- \quad (3)$$

H_2O_2 concentration measurement: The H_2O_2 concentration was measured by a traditional titanium sulfonate $Ti(SO_4)_2$ titration method based on the mechanism that a yellow solution of H_2TiO_4 was produced by H_2O_2 (equation (4)). Thus, the concentration of H_2TiO_4 can be measured by ultraviolet-visible spectroscopy. The wavelength used for the measurement was 408 nm.

$$Ti^{4+} + H_2O_2 + 2H_2O = H_2TiO_4 + 4H^+ \quad (4)$$

Therefore, the concentration of H_2O_2 (M) can be determined as M(H_2TiO_4).

The titanium sulfonate $Ti(SO_4)_2$ solution (2 mM) was prepared by dissolving 2 mmol $Ti(SO_4)_2$in 1 L 1 M H_2SO_4 solution. To quantify H_2O_2 concentration, 1 mL or 2 mL $Ti(SO_4)_2$ solution was added into 1 mL neutral or alkaline media, respectively. To obtain the calibration curve, H_2O_2 with known concentration was added to $Ti(SO_4)_2$ solution and measured by UV-vis (calibration curves in neutral and alkaline media are shown in Supplementary Fig. 17). Based on the linear relationship between the signal intensity and H_2TiO_4 concentration, the H_2O_2 concentration of the samples could be obtained.

Declarations

Acknowledgments

This work was supported by Ningbo S&T Innovation 2025 Major Special Program (2020Z059 and 2020Z107), BoXin project (BX20190339), Natural Science Founationg of Ningbo (No. 2019A610442 and 202003N4351)the China Postdoctoral Science Foundation (No. 2019M662127 and 2019M662124) and Hundred Talents Programs in Chinese Academy of Science. The DFT calculation is supported by the High-Performance Computing Center of Collaborative Innovation Center of Advanced Microstructures, Nanjing University.

Author contributions

W.X., Z.L (Zheng Liang), and Z.L (Zhiyi Lu). designed research; W.X., B.Z., and X.C. performed research; W.X., X.S., and Z.L. (Zhiyi Lu) contributed new reagents/analytic tools; F.S and H.W did the GC and TOC tests. S. G and Z.T did the DFT calculations; W.X., B.Z., X.C., X.S., and Z.L. (Zhiyi Lu) analyzed data; W.X., Z.L (Zheng Liang), N.H, Tanja Kallio, L.C and Z.L. (Zhiyi Lu) wrote the paper.

Additional information

Supplementary Information accompanies this paper at http://www.nature.com/naturecommunications

Competing financial interests: The authors declare no competing financial interests.

Reprints and permission information is available online at
http://npg.nature.com/reprintsandpermissions/

References

1 Edwards, J. K. H., Graham J Palladium and gold-palladium catalysts for the direct synthesis of hydrogen peroxide. *Angew. Chem. Int. Ed.* **47**, 9192-9198 (2008).

2 Perry, S. C. *et al.* Electrochemical synthesis of hydrogen peroxide from water and oxygen. *Nat. Rev. Chem.* **3**, 442-458 (2019).

3 Xia, C., Xia, Y., Zhu, P., Fan, L. & Wang, H. Direct electrosynthesis of pure aqueous H_2O_2 solutions up to 20% by weight using a solid electrolyte. *Science* **366**, 226-231 (2019).

4 Edwards, J. K. *et al.* Switching off hydrogen peroxide hydrogenation in the direct synthesis process. *Science* **323**, 1037-1041 (2009).

5 Samanta, C. Direct synthesis of hydrogen peroxide from hydrogen and oxygen: An overview of recent developments in the process. *Appl. Catal. A-Gen.* **350**, 133-149 (2008).

6 Yang, S. *et al.* Toward the decentralized electrochemical production of H_2O_2: a focus on the catalysis. *ACS Catal.* **8**, 4064-4081 (2018).

7 Yi, Y., Wang, L., Li, G. & Guo, H. A review on research progress in the direct synthesis of hydrogen peroxide from hydrogen and oxygen: noble-metal catalytic method, fuel-cell method and plasma method. *Catal. Sci. Technol.* **6**, 1593-1610 (2016).

8 Campos-Martin, J. M., Blanco-Brieva, Gema Fierro, Jose LG. Hydrogen peroxide synthesis: an outlook beyond the anthraquinone process. *Angew. Chem. Int. Ed.* **45**, 6962-6984 (2006).

9 Wang, Y., Waterhouse, G. I., Shang, L. & Zhang, T. Electrocatalytic Oxygen Reduction to Hydrogen Peroxide: From Homogenous to Heterogenous Electrocatalysis. *Adv. Energy. Mater.*, 2003323 (2020).

10 Rankin, R. B. & Greeley, J. Trends in selective hydrogen peroxide production on transition metal surfaces from first principles. *ACS Catal.* **2**, 2664-2672 (2012).

11 Lu, Z. *et al.* High-efficiency oxygen reduction to hydrogen peroxide catalysed by oxidized carbon materials. *Nat. Catal.* **1**, 156 (2018).

12 Jung, E., Shin, H., Hooch Antink, W., Sung, Y.-E. & Hyeon, T. Recent advances in electrochemical oxygen reduction to H_2O_2: catalyst and cell design. *ACS Energy Lett.* **5**, 1881-1892 (2020).

13 Sun, K. *et al.* Electrochemical oxygen reduction to hydrogen peroxide via a two-electron transfer pathway on carbon-based single-atom catalysts. *Adv. Mater. Interfaces*, 2001360 (2020).

14 Zhang, B., Xu, W., Lu, Z. & Sun, J. Recent progress on carbonaceous material engineering for electrochemical hydrogen peroxide generation. *Transactions of Tianjin University* **26**, 188-196 (2020).

15 Babuponnusami, A. & Muthukumar, K. Advanced oxidation of phenol: a comparison between Fenton, electro-Fenton, sono-electro-Fenton and photo-electro-Fenton processes. *Chem. Eng. J.* **183**, 1-9 (2012).

16 Brillas, E., Sirés, I. & Oturan, M. A. Electro-Fenton process and related electrochemical technologies based on Fenton's reaction chemistry. *Chem. Rev.* **109**, 6570-6631 (2009).

17 Nidheesh, P. & Gandhimathi, R. Trends in electro-Fenton process for water and wastewater treatment: an overview. *Desalination* **299**, 1-15 (2012).

18 Salimi, M. *et al.* Contaminants of emerging concern: a review of new approach in AOP technologies. *Environ. Monit. Assess.* **189**, 1-22 (2017).

19 Oturan, M. A. & Aaron, J.-J. Advanced oxidation processes in water/wastewater treatment: principles and applications. A review. *Crit. Rev. Environ. Sci. Technol.* **44**, 2577-2641 (2014).

20 Miklos, D. B. *et al.* Evaluation of advanced oxidation processes for water and wastewater treatment–A critical review. *Water Res.* **139**, 118-131 (2018).

21 Yamanaka, I. & Murayama, T. Neutral H_2O_2 synthesis by electrolysis of water and O_2. *Angew. Chem. Int. Ed.* **47**, 1900-1902 (2008).

22 Xia, B. Y. *et al.* A metal–organic framework-derived bifunctional oxygen electrocatalyst. *Nat. Energy.* **1**, 1-8 (2016).

23 Jiang, Y. *et al.* Selective electrochemical H_2O_2 production through two-electron oxygen electrochemistry. *Adv. Energy. Mater.* **8**, 1801909 (2018).

24 Xia, C., Kim, J. Y. T. & Wang, H. Recommended practice to report selectivity in electrochemical synthesis of H_2O_2. *Nat. Catal.* **3**, 605-607 (2020).

25 Li, F., Shao, Q., Hu, M., Chen, Y. & Huang, X. Hollow Pd-Sn nanocrystals for efficient direct H_2O_2 synthesis: the critical role of Sn on structure evolution and catalytic performance. *ACS Catal.* **8**, 3418-3423 (2018).

26 Jirkovský, J. S. *et al.* Single atom hot-spots at Au-Pd nanoalloys for electrocatalytic H_2O_2 production. *J. Am. Chem. Soc.* **133**, 19432-19441 (2011).

27 Edwards, J. K. *et al.* Direct synthesis of H_2O_2 from H_2 and O_2 over gold, palladium, and gold-palladium catalysts supported on acid-pretreated TiO_2. *Angew. Chem. Int. Ed.* **48**, 8512-8515 (2009).

28 Freakley, S. J. *et al.* Palladium-tin catalysts for the direct synthesis of H_2O_2 with high selectivity. *Science* **351**, 965-968 (2016).

29 Perazzolo, V. *et al.* Nitrogen and sulfur doped mesoporous carbon as metal-free electrocatalysts for the in situ production of hydrogen peroxide. *Carbon* **95**, 949-963 (2015).

30 Liu, Y., Quan, X., Fan, X., Wang, H. & Chen, S. High-yield electrosynthesis of hydrogen peroxide from oxygen reduction by hierarchically porous carbon. *Angew. Chem. Int. Ed.* **54**, 6837-6841 (2015).

31 Chen, S. *et al.* Designing boron nitride islands in carbon materials for efficient electrochemical synthesis of hydrogen peroxide. *J. Am. Chem. Soc.* **140**, 7851-7859 (2018).

32 Wood, K. N., O'Hayre, R. & Pylypenko, S. Recent progress on nitrogen/carbon structures designed for use in energy and sustainability applications. *Energy Environ. Sci.* **7**, 1212-1249 (2014).

33 Jiang, K. *et al.* Highly selective oxygen reduction to hydrogen peroxide on transition metal single atom coordination. *Nat. Commun.* **10**, 1-11 (2019).

34 Smith, P. T., Kim, Y., Benke, B. P., Kim, K. & Chang, C. J. Supramolecular Tuning Enables Selective Oxygen Reduction Catalyzed by Cobalt Porphyrins for Direct Electrosynthesis of Hydrogen Peroxide. *Angew. Chem. Int. Ed.* (2020).

35 Jung, E. *et al.* Atomic-level tuning of Co–N–C catalyst for high-performance electrochemical H_2O_2 production. *Nat. Mater.* **19**, 436-442 (2020).

36 Wang, Y. *et al.* High-Efficiency Oxygen Reduction to Hydrogen Peroxide Catalyzed by Nickel Single-Atom Catalysts with Tetradentate N_2O_2 Coordination in a Three-Phase Flow Cell. *Angew. Chem. Int. Ed.* **59**, 13057-13062 (2020).

37 Xu, W., Lu, Z., Sun, X., Jiang, L. & Duan, X. Superwetting electrodes for gas-involving electrocatalysis. *Acc. Chem. Res.* **51**, 1590-1598 (2018).

38 Lu, Z. *et al.* Superaerophilic carbon-nanotube-array electrode for high-performance oxygen reduction reaction. *Adv. Mater.* **28**, 7155-7161 (2016).

39 Zhang, Q. *et al.* Highly efficient electrosynthesis of hydrogen peroxide on a superhydrophobic three-phase interface by natural air diffusion. *Nat. Commun.* **11**, 1-11 (2020).

40 Feng, L. *et al.* Super-hydrophobic surfaces: from natural to artificial. *Adv. Mater* **14**, 1857-1860 (2002).

41 Sun, T., Feng, L., Gao, X. & Jiang, L. Bioinspired surfaces with special wettability. *Accounts. Chem. Res.* **38**, 644-652 (2005).

42 Ma, H. *et al.* Directional and Continuous Transport of Gas Bubbles on Superaerophilic Geometry-Gradient Surfaces in Aqueous Environments. *Adv. Funct. Mater.* **28**, 1705091 (2018).

43 Xu, W. *et al.* An advanced zinc air battery with nanostructured superwetting electrodes. *Energy Storage Mater.* **17**, 358-365 (2019).

44 Cai, Z. *et al.* Selectivity regulation of CO_2 electroreduction through contact interface engineering on superwetting Cu nanoarray electrodes. *Nano Res.* **12**, 345-349 (2019).

45 Jiang, K. *et al.* Isolated Ni single atoms in graphene nanosheets for high-performance CO_2 reduction. *Energy Environ. Sci.* **11**, 893-903 (2018).

46 Liu, W. *et al.* A Durable Nickel Single-Atom Catalyst for Hydrogenation Reactions and Cellulose Valorization under Harsh Conditions. *Angew. Chem. Int. Ed.* **130**, 7189-7193 (2018).

47 Zheng, T. *et al.* Large-scale and highly selective CO_2 electrocatalytic reduction on nickel single-atom catalyst. *Joule* **3**, 265-278 (2019).

48 Yang, S., Zhang, T., Li, G., Yang, L. & Lee, J. Y. Facile synthesis of N/M/O (M= Fe, Co, Ni) doped carbons for oxygen evolution catalysis in acid solution. *Energy Storage Mater.* **6**, 140-148 (2017).

49 Zhang, T. *et al.* Atomically Dispersed Nickel (I) on an Alloy-Encapsulated Nitrogen-Doped Carbon Nanotube Array for High-Performance Electrochemical CO_2 Reduction Reaction. *Angew. Chem. Int. Ed.* **132**, 12153-12159 (2020).

50 Torres, C. R., Crastechini, E., Feitosa, F. A., Pucci, C. R. & Borges, A. B. Influence of pH on the effectiveness of hydrogen peroxide whitening. *Oper. Den.* **39**, 261-268 (2014).

51 Iglesias, D. *et al.* N-doped graphitized carbon nanohorns as a forefront electrocatalyst in highly selective O_2 reduction to H_2O_2. *Chem* **4**, 106-123 (2018).

52 Nørskov, J. K. *et al.* Origin of the overpotential for oxygen reduction at a fuel-cell cathode. *J. Phys. Chem. B.* **108**, 17886-17892 (2004).

53 Yang, Q. *et al.* Atomically dispersed Lewis acid sites boost 2-electron oxygen reduction activity of carbon-based catalysts. *Nat. Commun.* **11**, 1-10 (2020).

54 Sirés, I., Brillas, E., Oturan, M. A., Rodrigo, M. A. & Panizza, M. Electrochemical advanced oxidation processes: today and tomorrow. A review. *Environ. Sci. Pollut. Res.* **21**, 8336-8367 (2014).

55 Yang, C., Xie, H., Wang, Z., Tan, Y. & Wang, N. Electro-Fenton Degradation of High Concentration Rhodamine B on Nickel Foam Cathode Catalyzed by Cucumber Bio-Templated Fe_3O_4@ PTFE. *Int. J. Electrochem. Sci* **16**, 151058 (2021).

56 Rezaei, F. & Vione, D. Effect of pH on zero valent iron performance in heterogeneous fenton and fenton-like processes: A review. *Molecules* **23**, 3127 (2018).

57 Zhang, Y. & Zhou, M. A critical review of the application of chelating agents to enable Fenton and Fenton-like reactions at high pH values. *J. Hazard. Mater.* **362**, 436-450 (2019).

58 Wang, N., Zheng, T., Zhang, G. & Wang, P. A review on Fenton-like processes for organic wastewater treatment. *J. Environ. Chem. Eng.* **4**, 762-787 (2016).

59 Liang, L. *et al.* Novel rolling-made gas-diffusion electrode loading trace transition metal for efficient heterogeneous electro-Fenton-like. *J. Environ. Chem. Eng.* **4**, 4400-4408 (2016).

60 Yao, Y. *et al.* Fe, Co, Ni nanocrystals encapsulated in nitrogen-doped carbon nanotubes as Fenton-like catalysts for organic pollutant removal. *J. Hazard. Mater.* **314**, 129-139 (2016).

Figures

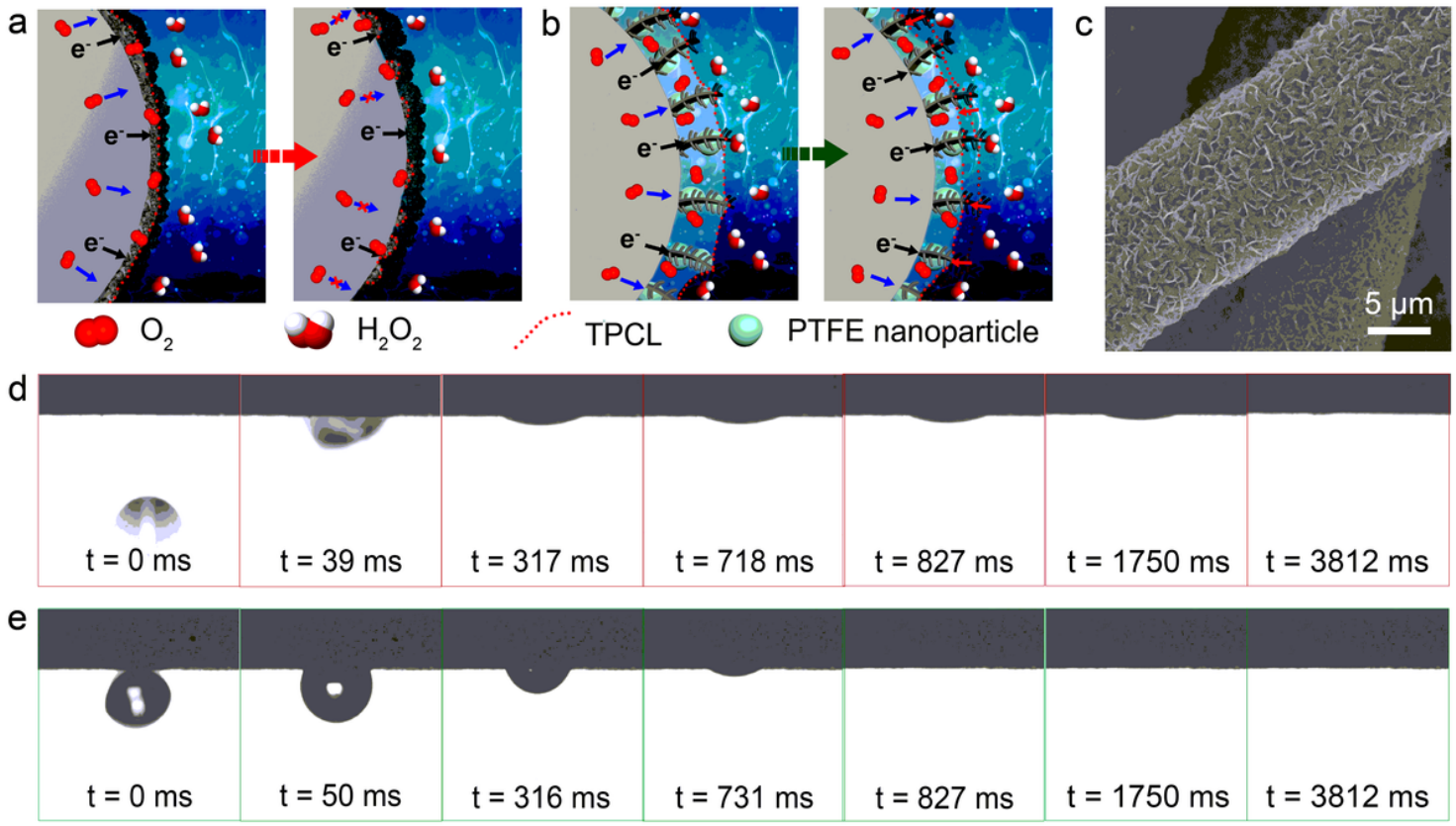

Figure 1

(a-b) Schematic illustration of surface properties of conventional gas-diffusion electrode and superaerophilic electrode before and after long-term electrochemical oxygen reduction to H2O2; (c) typical SEM image of NiOC electrode (scale bar: 5μm); (d-e) air bubble adhesion behaviors on D-NiOC (d) and IS-NiOC (e) electrode under neutral electrolyte.

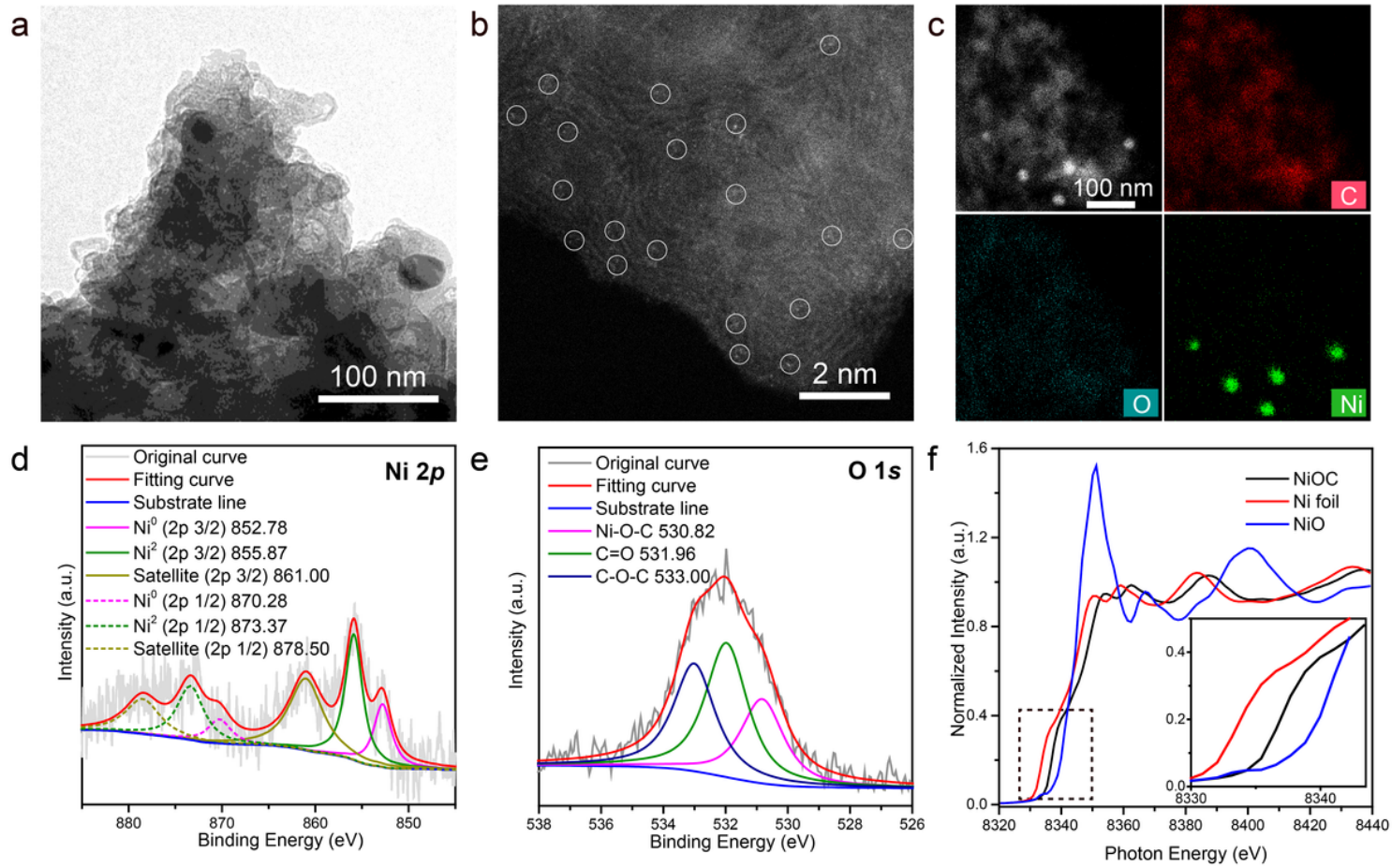

Figure 2

(a-b) High-resolution TEM (scale bar: 100 nm) and aberration-corrected HAADF-STEM (scale bar: 2 nm) images of NiOC catalyst; (c) STEM-EDX mapping results of NiOC catalyst (scale bar: 100 nm); (d-e) high-resolution XPS spectra of Ni 2p and O 1s in NiOC electrode; (f) Ni K-edge XANES spectra in NiOC electrode.

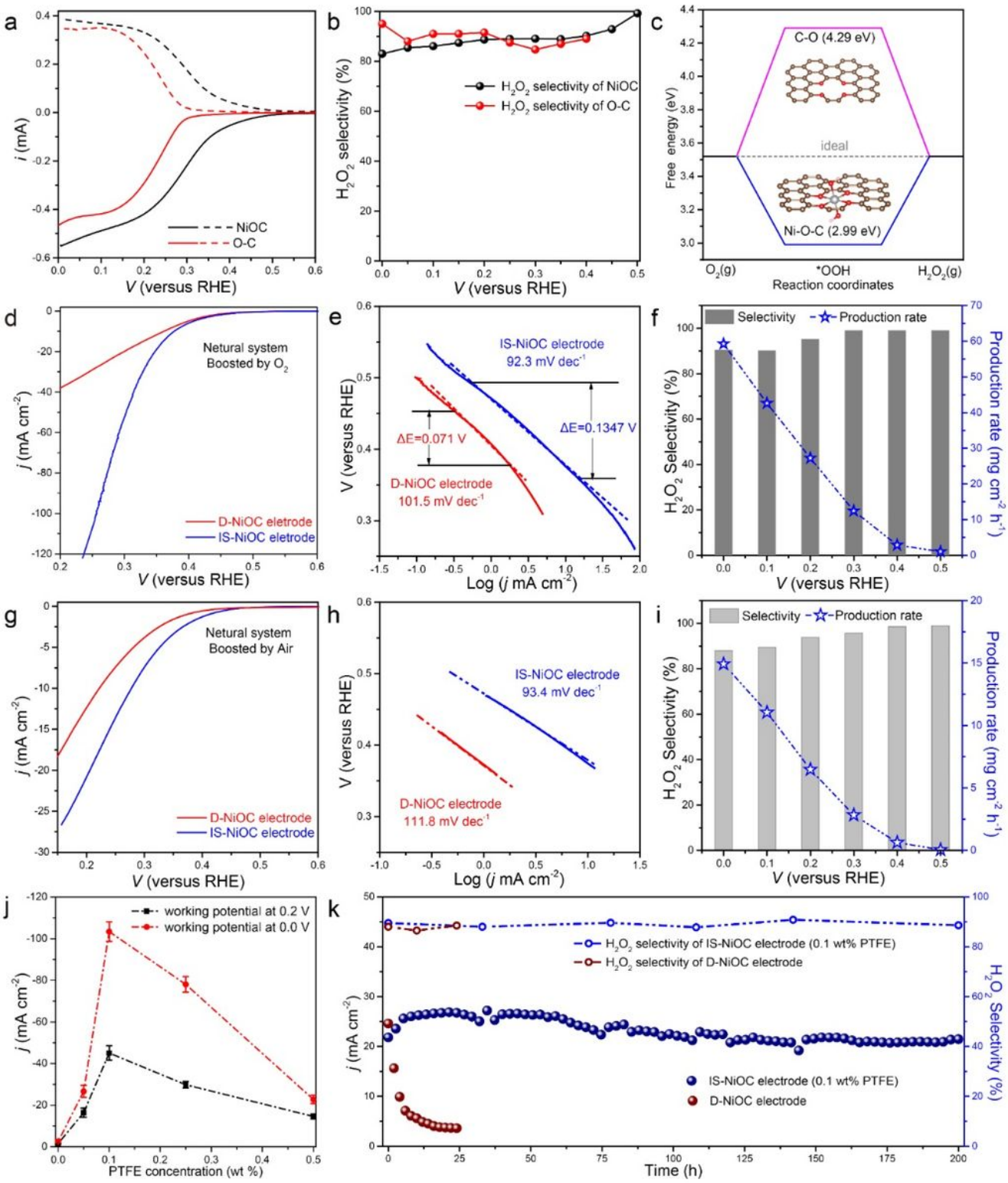

Figure 3

(a) Electrochemical oxygen reduction polarization curves at 1,600 r.p.m. (solid lines) and simultaneous H2O2 detection currents at the ring electrode (dashed lines) for the NiOC catalyst and O-C catalyst in 0.1 M PBS solution; (b) relevant calculated H2O2 selectivity; (c) free energy diagram of 2e ORR on NiOC and O-C at equilibrium potential of the reaction; (d) LSV curves (with IR-correction) of IS-NiOC electrode and D-NiOC electrode recorded in 1 M Na2SO4 solution with oxygen-bubbling; (e) corresponding Tafel slopes of

IS-NiOC and D-NiOC electrodes; (f) corresponding selectivity and production rate of IS-NiOC electrode; (g-i) relevant performance of IS-NiOC and D-NiOC electrodes under air reduction; (j) current density in oxygen atmosphere varieties with the PTFE concentration; (k) long-term stability and selectivity of IS-NiOC and D-NiOC electrodes for H2O2 production.

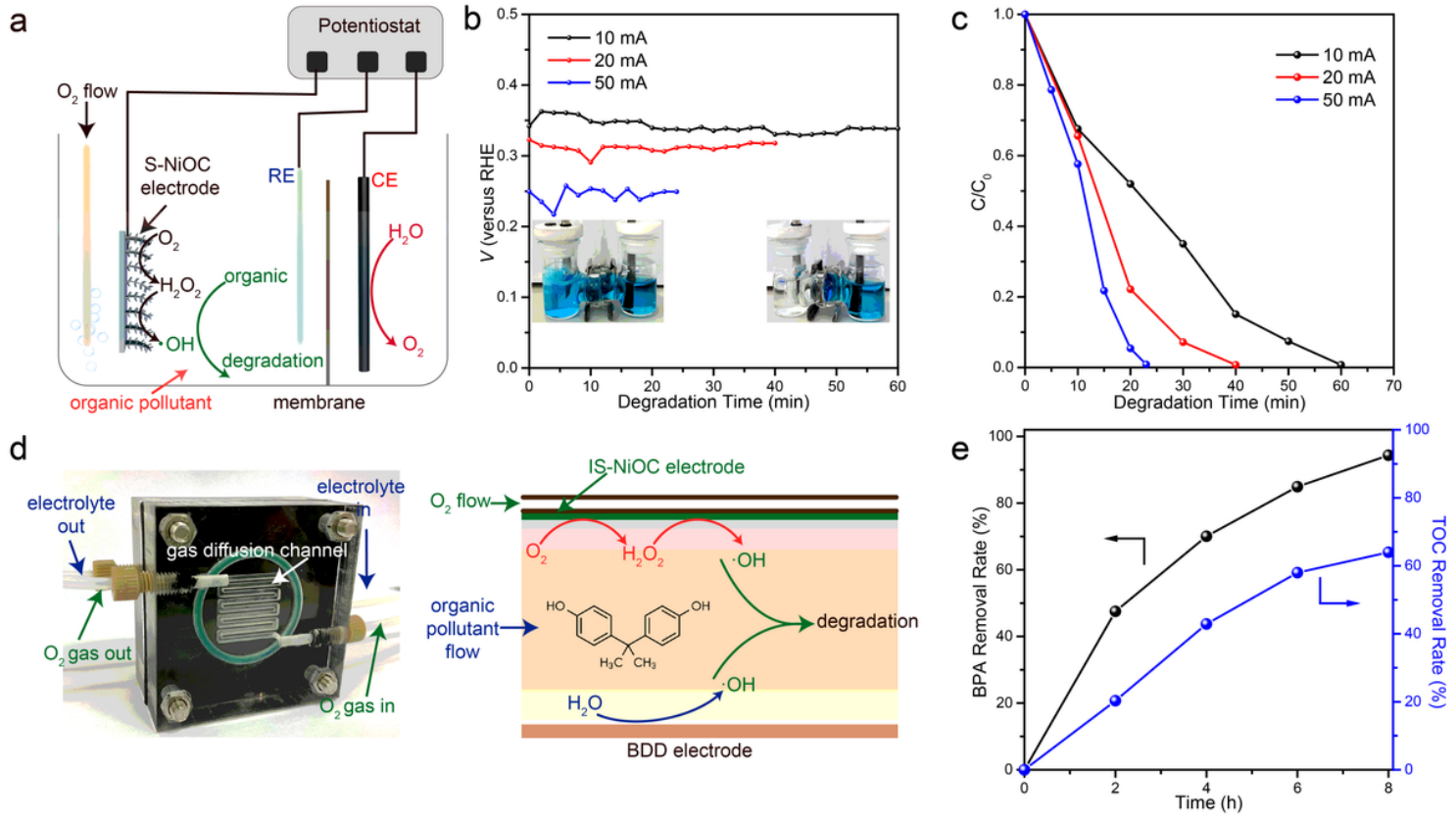

Figure 4

(a) Schematic illustration of 3-electrode steady-state device for organic degradation; (b-c) operation voltages and degradation rates under different currents (conditions: 0.05 M Na2SO4, 50 mg/L Indigo, oxygen gas flow rate 80 sccm); (d) schematic illustration of flow state device, where the IS-NiOC and BDD electrode were employed as the cathode and anode, respectively; (e) BPA and TOC removal rates of the device constructed by IS-NiOC and BDD electrode electrodes (conditions: 0.05 M Na2SO4, 50 mg/L BPA, oxygen gas flow rate was 80 sccm, electrolyte recycle flow rate was 2 mL min-1, the volume of the circulating solution was 50 mL).

Supplementary Files

This is a list of supplementary files associated with this preprint. Click to download.

- SupplementaryMovie1.mkv
- SupplementaryMovie2.mkv
- supportinginformationSNOC.pdf